Nuclear Instruments and Methods in Physics Research A 368 (1996) 617-627

NUCLEAR INSTRUMENTS & METHODS IN PHYSICS RESEARCH Section A

ELSEVIER

# Design and performance of a cesium iodide detector

T. Adams [a], J.M. Bishop [a], R. Cady [a], N.M. Cason [a,*], J. Gress [a,1], C. Kopp [a], J.M. LoSecco [a], J.J. Manak [a], A.H. Sanjari [a], W.D. Shephard [a], D.L. Stienike [a], S.A. Taegar [a], D.R. Thompson [a], S.U. Chung [b], R.W. Hackenburg [b], C. Olchanski [b], D.P. Weygand [b], H.J. Willutzki [b], S. Denisov [c], A. Dushkin [c], V. Kochetkov [c], I. Shein [c], A. Soldatov [c], B.B. Brabson [d], R.R. Crittenden [d], A.R. Dzierba [d], J. Gunter [d], R. Lindenbusch [d], D.R. Rust [d], E. Scott [d], P.T. Smith [d], T. Sulanke [d], S. Teige [d], Z. Bar-Yam [e], J.P. Dowd [e], P. Eugenio [e], M. Hayek [e,2], W. Kern [e], E. King [e], N. Shenhav [e,1], V.A. Bodyagin [f], A.M. Gribushin [f], M.A. Kostin [f], V.L. Korotkikh [f], A.I. Ostrovidov [f], A.S. Proskuryakov [f], L.I. Sarycheva [f], N.B. Sinev [f], I.N. Vardanyan [f], A.A. Yershov [f], D.S. Brown [g], T.K. Pedlar [g], K.K. Seth [g], J. Wise [g], D. Zhao [g], G.S. Adams [h], J. Napolitano [h], M. Nozar [h], J.A. Smith [h], M. Witkowski [h]

[a] *Department of Physics, University of Notre Dame, Notre Dame, IN 46556, USA*
[b] *Brookhaven National Laboratory, Upton, L.I., NY 11973, USA*
[c] *Institute for High Energy Physics, Protvino, Russian Federation*
[d] *Department of Physics, Indiana University, Bloomington, IN 47405, USA*
[e] *University of Massachusetts Dartmouth, North Dartmouth, MA 02747, USA*
[f] *Institute for Nuclear Physics, Moscow State University, Moscow, Russian Federation*
[g] *Northwestern University, Evanston, IL 60208, USA*
[h] *Rensselaer Polytechnic Institute, Troy, NY 12180, USA*

Received 12 June 1995

**Abstract**

The design, construction, and performance of a 198-element CsI detector built for Brookhaven experiment E852 is described. Design considerations for the array included such factors as rate, magnetic field, sensitivity and acceptance. Signals were obtained with a photodiode/preamplifier combination using PIN photodiodes. Data were taken over the course of two runs during the summers of 1993 and 1994. A calibration procedure using halo muons is described. The gain, energy resolution, and position resolution of the detector are discussed. Finally, the ability of the detector to be used as a low energy photon veto is illustrated using the data.

## 1. Introduction

Brookhaven experiment E852 has been under design and construction for several years and had its first large-scale data run in the summer of 1994. The purpose of the experiment is to search for exotic mesons such as glueballs, hybrids, and multiquark states. The experiment will concentrate on the study of meson states in the 1–3 GeV/$c^2$ mass range that decay into 0–4 charged particles plus photons. Located in the multiparticle spectrometer (MPS) magnet facility at the AGS, E852 represents a significant upgrade to this facility with the addition of a 3045-element lead-glass detector (LGD [1]) and a thallium-doped cesium iodide detector.

The data from E852 are expected to be characterized by many overlapping resonances in the 1–3 GeV/$c^2$ mass range. In order to obtain spin-parity and production information about possible new states, detailed partial wave analyses of the data will be required. Such analyses are valid only when exclusive production amplitudes can be isolated; contamination of the data by events with missing $\pi^0$'s can invalidate these analyses. Since the resolution of the spectrometer is not always good enough to reliably remove this contamination from the data sample by a missing-mass cut, an efficient detector which can tag the presence of photons (from

* Corresponding author. Tel. +1 219 631 6305, fax +1 219 631 5952, e-mail cason@undhep.hep.nd.edu.

[1] Moorhead State University, Moorhead, MN 56563.

[2] Rafael, Haifa, Isreal.


*SSDI* 0168-9002(95)00668-0

the decay of $\pi^0$'s) which miss the LGD is essential for the experiment. CsI detectors have been used in other experiments for photon detection [2–4]. This report describes the design, construction, and operating characteristics of a new CsI detector constructed to do this tagging.

## 2. Experimental arrangement

The spectrometer, which is located in the A1 beam line at Brookhaven, is shown schematically in Fig. 1. and consists of three parts. The first part is the target region (designated as **T** in Fig. 1) which is located near the center of the 1.0 T MPS magnet and is discussed in detail below. The second part is the charged-particle tracking region downstream of the target, still within the magnet. This consists of proportional chambers **P1**, **P2** and **P3**; drift chambers **D1–D6**; and a picture-frame lead/scintillator-sandwich photon veto **V**. Finally, the photon calorimeter region downstream of the magnet consists of a Cherenkov counter **C** (to be constructed), a large proportional chamber **TDX**, and the lead-glass hodoscope **LGD**.

Details of the target region are shown in Fig. 2. A 30-cm long liquid hydrogen target is surrounded by a cylindrical drift chamber (CDC) which is itself surrounded by the CsI detector. The CsI detector (called CID) consists of two parts: a CsI Barrel (CIB) of 10 rings with 18 crystals per ring; and a single upstream 18-crystal CsI Ring (CIR) with somewhat larger crystals than those in the barrel. A unique scintillation counter which was designed to be placed downstream of the hydrogen counter and which has been previously described [5] was not installed for the 1994 run.

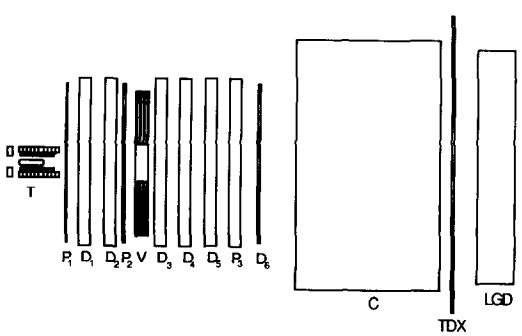


Fig. 1. Diagram of the E852 spectrometer. The target region (T), proportional chambers $P_1$–$P_3$, drift chambers $D_1$–$D_6$, and lead-scintillator window frame veto V are located within the 1.0 T magnetic field of the multi particle spectrometer (MPS). The lead glass hodoscope (LGD) and large drift chamber TDX are located downstream of the magnet. Cherenkov counter C is not yet installed in the experiment.

## 3. Cesium iodide detector design and construction

### 3.1. Design considerations

Several designs were considered for the soft-photon veto in this experiment. These included a lead-scintillator sandwich detector, a BGO detector, and a CsI(Tl) detector. The lead-scintillator soft photon veto design used in the GAMS experiment [6] achieved a high sensitivity to photons only above 250 MeV. Our own studies of the lead-scintillator design showed that it would be extremely difficult to get good sensitivity with that design for photons below 50 MeV.

A barrel consisting of scintillation crystals has several advantages over a lead-scintillator design, including higher sensitivity and greater ease of segmentation. With a large number of relatively small crystals one can obtain some energy and position information that could be useful in later analysis.

Thallium-doped cesium iodide was chosen over BGO crystals because of its lower cost per unit radiation length, its emission spectrum well matched to photodiodes and its high light output per unit of energy deposited (52000 photons/MeV [7]). The higher density and faster response time of BGO did not outweigh its lower light output, higher cost per unit radiation length and emission spectrum poorly matched to photodiodes. (Photodiode readout of the crystals was necessary because of the presence of the detector in the 1 T magnetic field of the MPS which ruled out the use of photomultipliers.)

Typical background in the data is expected to come from

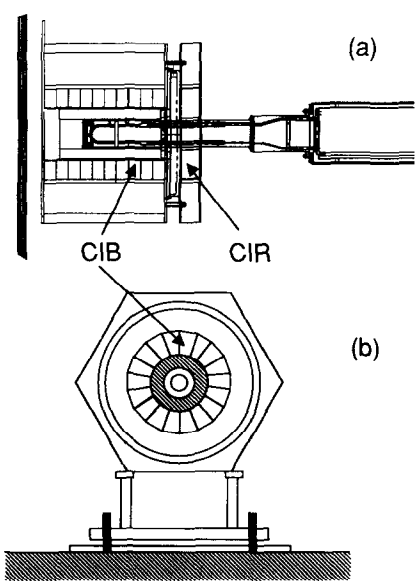


Fig. 2. Diagram of the E852 target region. Shown are elevation views from (a) the side and (b) the end. Indicated are the single upstream ring (CIR) and the barrel of CsI crystals (CIB).

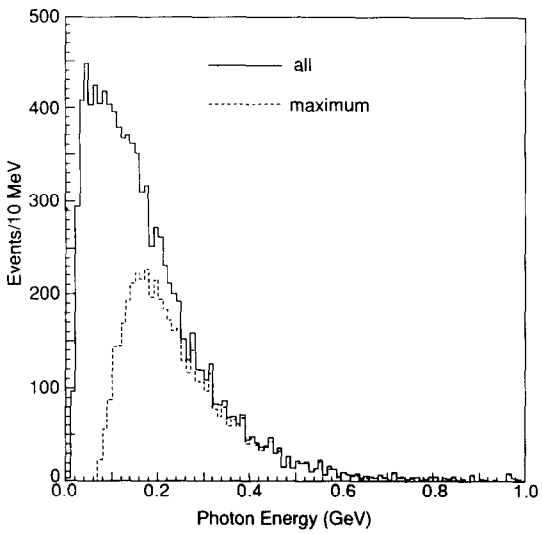


Fig. 3. Photon energy distribution from $\pi^0$ decay for events of the type $\pi^- p \rightarrow \Delta^0(1236)X^0 \rightarrow n\,\pi^0\,X^0$ at 18 GeV.

reactions such as $\pi^- p \rightarrow \Delta^0(1236)X^0 \rightarrow n\,\pi^0\,X^0$ where the photons from the $\pi^0$ decay of the $\Delta^0$ (the "soft $\pi^0$") do not hit the LGD. To study this process we generated Monte Carlo events with a beam momentum of 18 GeV/$c$, an $X^0$ mass of 1.400 GeV/$c^2$, and a peripheral four-momentum-transfer variation of the form $e^{-7|t|}$. The energy distribution of the photons (two entries per event) from the soft $\pi^0$ decay in the reaction is shown as the solid histogram in Fig. 3. The dashed histogram shows the distribution of the most energetic photon per event. The overall photon distribution rises rapidly with energy, beginning at about 10 MeV, to a peak around 45 MeV. As one notes in the dashed histogram, most events contain at least one photon with energy greater than 100 MeV. A detector designed to veto these events must be able to detect at least one photon from these decays. Ideally, it should be sensitive enough to respond to the lowest energy photons.

The design of a photon detector for these events must take into account the low-energy behavior of the photon attenuation length. A plot of this attenuation length for CsI(Tl) is shown in Fig. 4 [8]. Although the asymptotic (high energy) value of $\ell = 2.38$ cm is achieved at about 10 GeV one notes that the value between 1 and 30 MeV is above 4 cm, thus lowering the detection efficiency in this energy range.

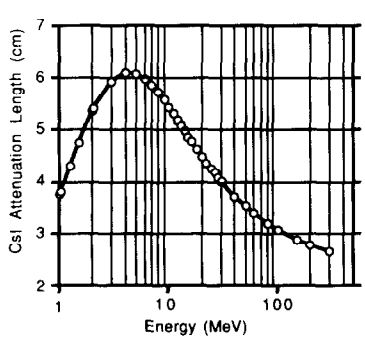


Fig. 4. Attenuation length vs. energy in CsI(Tl).

The light output from CsI(Tl) is known to be rather slow, with a rise time of about 0.1 $\mu$s and a fall time of 1 $\mu$s. With an expected beam rate in our experiment of about 2 MHz, care was taken to be sure that the rates in a single crystal would not be so great that pile-up would be a problem. Interactions in either the target region or the beam halo region can lead to high rates in the detector. During data taking, the CID detector is located in the MPS magnet beginning at a radial distance of 11 cm from the center of the target. At a beam momentum of 18 GeV/$c$, the overwhelming number of produced particles exit the downstream end of the target and do not strike CID. A worst-case scenario for pile-up is given by assuming that the full interaction rate in the target (3% of a 2 MHz beam) yields interactions which produce two photons striking the barrel (i.e. every event has a slow $\pi^0$). In this case, an average photon rate of 0.6 kHz will be present on each crystal. For an average crystal hit multiplicity of 5 crystals per photon (as estimated using Monte Carlo simulations), the average rate is of the order of 3 kHz/block.

Rate due to halo is more difficult to estimate and it has a more pronounced effect on the CsI since many halo tracks pass along the length of the CsI hitting all eleven rings of the detector. If the halo rate is 10% of the beam intensity and is distributed uniformly over a one-meter radius centered on the beam, a rate of 4 kHz due to halo is incident on the barrel. The total rate in each crystal would in this case be about 0.2 kHz or 1/18th of the total rate (recall that there are 18 rows of crystals). During the 1993 and 1994 data runs the rate above a threshold of ~20 MeV was determined to be between 2 kHz and 5 kHz for most crystals.

Since the detector was intended to be used in a veto mode, pile-up in any one of the 198 crystals could potentially cause a loss of data during the final analysis. A compromise was achieved between energy resolution and loss due to pile-up. At the highest beam intensities, up to one third of the data was lost due to pile-up while a sensitivity of better than 20 MeV was achieved.

The inner radius (11 cm) of CIB was chosen to be as small as possible with the constraint that charged particles produced in reactions of interest be unlikely to hit the barrel (leading to scattering and loss of events). The size was required to be large enough to allow for the installation of a cylindrical drift chamber (CDC) nested inside CIB and used to detect recoil protons. With the 11 cm radius, 97% of the outgoing pions in the reaction $\pi^- p \rightarrow p M^-(1405) \rightarrow p\eta^0\pi^-$ at 18 GeV and 1.0 T magnetic field exit the target region without hitting CIB. The location of the downstream end of CIB was chosen so that a photon produced at a large enough angle to miss both the lead glass detector and the picture-frame veto V, would pass through at least four radiation lengths of CsI(Tl). The outer radius of the barrel was

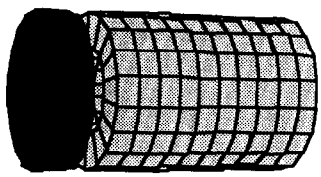

Fig. 5. Diagram of the CsI(Tl) detector CID showing the upstring ring (CIR) and the downstream barrel (CIB).

chosen so that the radial thickness of the barrel was 7.5 cm (4 radiation lengths).

The length of the CIB blocks along the beam (the $z$ direction) was chosen to be 5 cm to balance the conflicting requirements of minimizing shower sharing between individual crystals (the Molière radius of CsI(Tl) is 3.8 cm) and of reducing the individual ring exposure rate.

The upstream ring, CIR, was chosen to be as hermetic as possible in the presence of the beam pipe, the CDC electronics, and the hydrogen target. GEANT [9] studies indicated that the precise size, configuration, and position of the CIR would not be critical since it contributed only about 3% to the overall efficiency. It was decided that the CIR would consist of a single ring with outer diameter equal to that of CIB, inner diameter of 11.5 cm to match the target diameter, and $z$-length of 7.5 cm, equal to the radial thickness of a CIB ring. CIR is displaced 6 cm from the upstream end of CIB to allow room for the CDC readout electronics.

### 3.2. Construction

The CID consists of two parts, a barrel and an upstream ring, designated CIB and CIR, respectively. CIB consists of 10 rings of 18 crystals each. All crystals have the shape of a truncated wedge. CIR consists of a single ring of 18 crystals of a shape similar to those of CIB, but with larger dimensions in both the beam and the radial directions, and is located upstream of CIB and the hydrogen target. The CIR crystals and electronics are located in a separate container to allow easy access to the cylindrical drift chamber CDC inside CIB. A schematic drawing of CID is shown in Fig. 5.

The specified physical dimensions and tolerances for the CIR and CIB crystals are listed in Table 1 and illustrated in Fig. 6. The quoted dimensions include crystal wrapping. All crystal faces, except the outside face ($L2 \times W$), were left unpolished and were wrapped in three layers of teflon tape (a diffuse reflector) and an outer layer of aluminized mylar to maximize light collection at the photodiode. The outside face was polished to maximize light transmission to the photodiode attached to it. In order to ensure that physical specifications were met, Notre Dame provided each supplier with precision-machined gauge blocks. However, after initial shipments consistently failed to meet the specifications as measured using the gauge blocks, it was decided that subsequent shipments would consist of crystals in groups of 18 that fit a template of the ring dimensions. This arrangement proved satisfactory.

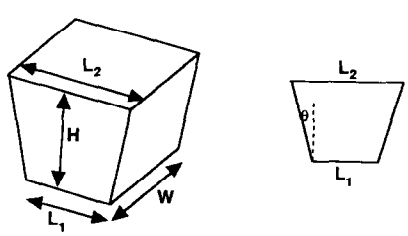


Fig. 6. Diagram of a CsI crystal. Dimensions for the two types of blocks are given in Table 1.

To measure the performance of the CsI(Tl) crystals, a combined $^{137}$Cs and $^{60}$Co pulse height spectrum was taken for each crystal. The test setup consisted of a light-tight box in which each crystal was optically coupled to a Thorn EMI 9939B03 photomultiplier tube using a silicone rubber compound pad [10]. To ensure uniformity of the coupling from crystal to crystal, a spring-loaded holder was used to apply pressure at the interface. The duration of the run was computer controlled and the $^{137}$Cs and $^{60}$Co pulse height spectra were taken simultaneously using the LeCroy Model 3001 qVt Multichannel Analyzer. A typical pulse height spectrum is shown in Fig. 7. The relative light output was determined from the positions of the $^{137}$Cs 0.662 MeV peak, the $^{60}$Co 1.17 MeV peak and the pedestal. The resolution was then obtained from the width of the 0.662 MeV peak.

Testing was conducted in a series of runs extending over a year, the delivery time period. To obtain a measure of the uniformity of the crystals, the gain of each crystal was normalized to the average gain of a standard crystal measured over the course of each run. An estimate of the stability of

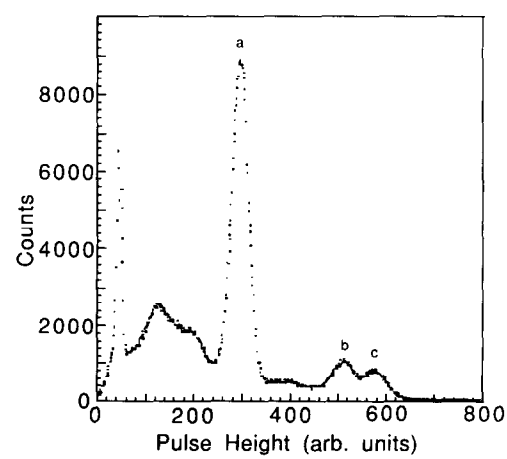


Fig. 7. Combined $^{137}$Cs and $^{60}$Co pulse height spectrum used to evaluate the CsI(Tl) crystal performance. The peaks labelled a, b, and c are the 0.662 MeV, 1.17 MeV and 1.33 MeV peaks due to $^{137}$Cs, $^{60}$Co and $^{60}$Co, respectively.

Table 1
Dimensions of the CsI Crystals

| Crystal Type | $L1$ [cm] | $L2$ [cm] | $W$ [cm] | $H$ [cm] | $\theta$ (°) |
|---|---|---|---|---|---|
| CIB | 3.879(.01) | 6.524(.01) | 5.000(.01) | 7.500(.1) | 100 |
| CIR | 2.015(.01) | 6.524(.01) | 7.500(.01) | 12.785(.1) | 100 |

the system over time is given by the gain distribution for this standard crystal and is of the order of ±2.5%.

Plots of the distribution in normalized output, the resolution, and the normalized output versus resolution for all crystals except those initially returned due to physical specification failure, are shown in Fig. 8. Note that the crystals with the highest light output also have the best resolution. Crystals that had an output below 400 ch/MeV were rejected. During the testing, some correlation between the appearance of a crystal and its performance was noted. In particular, crystals of lower output and poorer resolution tended to be "off-color", tinted either slightly pink, green, or brown.

The crystals in the barrel were arranged around a 106-mm I.D. aluminum tube 2 mm thick. (See Fig. 2b.) A thin layer of foam (approximately 2 mm thick) was placed around the tube to provide a soft support for the inner crystal bases. Eighteen aluminum spines running the length of the barrel formed a cage-like structure that supported the crystals and the associated electronics in the barrel. Dry nitrogen was passed through the barrel to protect the crystals from moisture. A silicone gel pad was placed on each crystal to provide an optical contact with an electronics module containing a photodiode. All of the power, gas and signal lines were sent through one of six piano-hinged doors which provided access to the interior electronics.

For nine of the ten barrel rings, electronics modules serviced 3 crystals each. Each module contained a three-channel preamplifier, drivers, and 3 photodiodes that were mounted inside the barrel directly above 3 of the crystals in a row. The final assembly consisted of 54 modules containing 3 diodes each and, in addition, 36 modules containing a single diode attached to a single crystal for use in the 10th ring of CIB and in CIR. Each diode was seated on a 1/4 in. thick Teflon plate, with the pins of the diode passing through the plate to sockets mounted on a PC board. Teflon was chosen as a building material both for its low leakage current and because it is an excellent diffuse reflector. The two-layer Teflon printed circuit board had a power socket and a connector to provide the preamplifier signal to the driver board. The entire module containing Teflon, PC board, and driver could be easily removed from the barrel in the event of failure. In addition, the module itself could be easily taken apart to replace a driver, PC board or diode. A drawing of a single channel module seated inside the barrel is shown in Fig. 9.

### 3.3. Electronic design

The signal from the CsI follows the schematic block diagram shown in Fig. 10. Each of the 198 channels consists of: a Hamamatsu type 3590-01 1-cm$^2$ photodiode mounted on the face of each crystal; a modified eV Products [11]

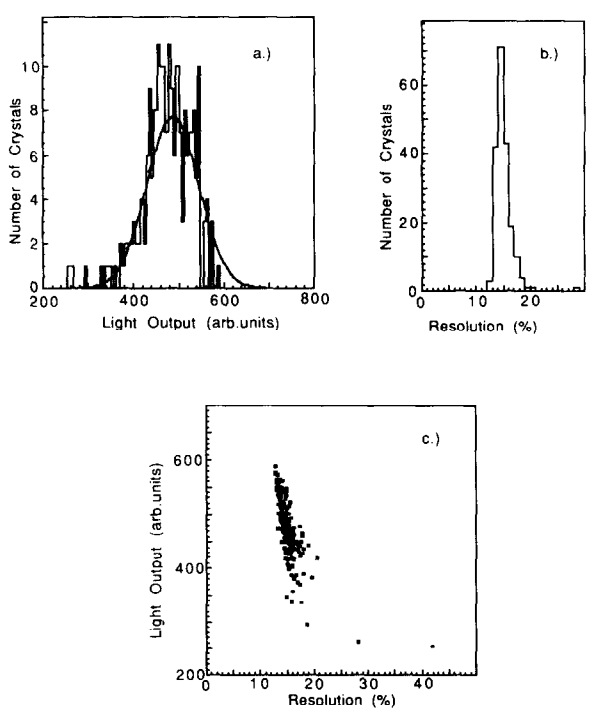


Fig. 8. Plots of (a) the distribution in normalized light output, (b) resolution and (c) normalized light output vs. resolution for the CsI(Tl) crystals.

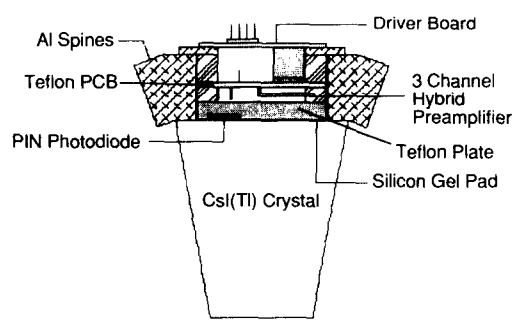


Fig. 9. Schematic drawing of a single CsI module (viewed along the beam) as assembled within the detector.

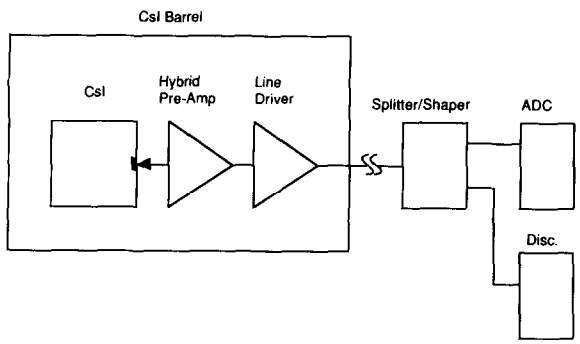


Fig. 10. Electronics block diagram for the CsI detector.

3-channel preamplifier; a driver based on an Analog Devices type 827JN op amp; a custom-made splitter-shaper board; a LeCroy 1881 ADC; and a LeCroy 4413 discriminator. The pulse height for each channel is discriminated and OR'ed with all the other channels for use as part of the second level trigger in the experiment. In addition the signal for each channel is integrated and digitized for off-line analysis. The electronics for the single and triple channel modules is identical.

PIN-type Hamamatsu 3590-01 photodiodes were selected for use with the crystals. These diodes have a 100-$\mu$m thick depletion layer and a 1 cm×1 cm active area. These photodiodes were chosen for their low dark current and low cost.

Each photodiode was tested using a $^{241}$Am source. The diode was placed 1 cm from a source located inside a small aluminum light-tight container. A modified eV Products single-channel high-gain preamplifier was used to amplify the diode signal. A 40-V bias was applied to the diode and the preamplifier signal was fed to a 2003BT Canberra spectroscopy amplifier with a 2-$\mu$s shaping time. The spectrum was recorded by a LeCroy qVt and for each photodiode the position, width, and gain of the 60 keV peak were obtained. With the exception of one, all diodes were essentially identical within the accuracy of our study. A typical diode spectrum in shown in Fig. 11. During an integrated running period of roughly six months in 1993 and 1994 none of the 198 diodes in CID failed.

The design of the electronics for the CsI barrel was a compromise between sensitivity and rate capability. Each pulse from the charge-sensitive preamplifier has a rise time of 1.4 $\mu$s and a fall time of about 40 $\mu$s. The fall time is important because a long value could lead to pile-up on the preamplifier and a short value would reduce the sensitivity of the detector. Three preamplifiers were surface mounted on a small hybrid board manufactured by eV Products. The manufacturer's specification for the preamplifiers included: a sensitivity of 2 mV/fC; cross-talk of less than 1% between hybrid channels; and a variation in gain between channels of less than 10%. The hybrid was not able to drive the 50 Ω signal cables directly and thus the use of a separate driver board was required.

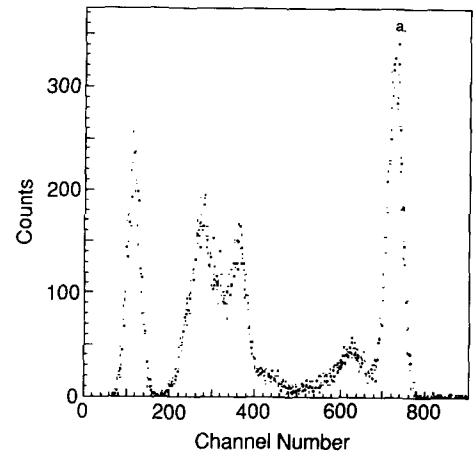


Fig. 11. Typical pulse height spectrum of a Hamamatsu 3590-01 photodiode with an $^{241}$Am source. The peak labelled (a) is the 60 keV $^{241}$Am peak.

Each hybrid was socketed into a 14.5 cm×4.9 cm Teflon printed circuit board which also received the power, bias, and diode input circuits. The boards also provided a mechanical structure to hold the photodiodes above their respective crystals. Power (+6 V, −12 V) and bias (+40 V) were distributed to each board by a 10-pin ribbon cable fed by a small custom-made power-distribution board on the upstream end of the barrel. Care was taken in the layout of the board to avoid oscillations and cross talk, potential difficulties due to the sensitivity of the hybrid. The two-layer board had extensive ground planes and the hybrid was mounted on the underside of the board facing the crystals to avoid cross talk. All low-impedance output signals were handled on the upper layer of the board, and kept as far as possible from the input signals on the underside of the board. Surface-mount technology was also used, since it too reduced feedback on the board. The cross talk between channels was measured for all of the boards and was no more than 2% for a given hybrid/board combination. Modified printed circuit boards based on the same hybrids were made for CIR and the first ring of CIB since three-channel boards would not fit in those locations. All inputs and outputs were capacitively coupled.

The driver circuit was based on the Analog Devices type 827JN dual op amp. It was mounted on a separate board directly above the preamplifier board to reduce feedback between the hybrid and the driver. The op amp had an input impedance of 22.1 kΩ and a capacitively coupled 1 $\mu$F output to remove any possible DC offset due to possible unequal balancing of the op amp.

The signals from the driver boards were carried by 180 ft of 50-Ω coaxial cables to an electronics hut where they were fed into splitter-shaper boards located in a standard NIM crate in an electronics rack. The purpose of these boards was to provide a signal to both the ADCs and discriminators. Each splitter-shaper module contained 16 Lemo inputs and 16 Lemo outputs on the front panel and a 100-Ω 34-pin

connector on the rear. The pulse to the ADCs was shortened by a 0.1-$\mu$F in-line capacitor and sent through the 34-pin connector at the rear of the module. A 5 ft 100-$\Omega$ twisted pair ribbon cable carried the signal to a LeCroy model 1810 ADC. The signal to the discriminator was sent through a buffer amplifier and was shaped by passage through a Butterworth filter. The resulting pulse was then amplified by a factor of 25 and was accessed by a front-panel Lemo connector. The amplified and shaped signal for each of the 198 channels was then sent to a LeCroy 4413 discriminator for use in a second-level trigger.

During the test run in 1993 it was noted that many of the channels were susceptible to an oscillation with a magnitude of up to 10 MeV energy equivalent and a frequency of 360 Hz. The problem was intermittent. It was suspected that the problem was caused by a ground loop, and a poorly grounded electronics hut. The splitter/shaper boards, power supplies and ADCs were moved to a different electronics trailer in 1994. Care was taken to insure that the ground at the detector was the same as for the ADCs and the power lines were rerouted to follow the same path as the shielded signal cables. No oscillations were observed during the 1994 data run.

Over an integrated running period of 6 months, there was no observed failure of any electronic components (hybrid, driver, splitter/shaper). The only failure mode observed was caused by loose Lemo-style connectors on the cables connecting to the face of the splitter-shaper modules. Typically, 5–10 cables would be loose at the beginning of a running period. After tightening, the channels would usually work without further attention for the duration of the run.

### 3.4. Monitoring and calibration system

For monitoring and calibration purposes, beam-halo counters were constructed. (See the discussion below on the response of the CsI crystals to halo muons.) These counters were positioned on the upstream and downstream ends of the barrel and were put into a coincidence circuit. Each halo counter consisted of a sheet of BC400 scintillator cut so as to cover a 120° segment of a ring of crystals or six crystals of the 18 in a ring. A Hamamatsu type R2490-01 photomultiplier capable of operating in a high magnetic field was used on each of the counters and care was taken to orient each tube with respect to the MPS magnet field so as to assure maximum gain. The upstream and downstream halo counters were offset by 60° so that a coincidence would correspond to a halo particle traversing an angular segment of 60° that contained three crystals in each ring.

Before each spill a single pedestal value was recorded for each CID channel. The central value of the pedestal spectrum determined the appropriate ADC value for zero energy for each channel, and the width (sigma) of the distribution determined the electronic noise. The magnitude of the width for each channel corresponded to about 500 keV of energy deposited in the crystal.

The central value of the pedestal and the width were monitored throughout the run. The widths remained constant over the six months of the 1994 run, showing an average shift of only 2 ADC counts. This shift corresponds to only a quarter millivolt increase in RMS noise for all channels over a 6-month period.

## 4. Detector performance

### 4.1. Response to minimum ionizing particles

Beam halo is used in the experiment to calibrate and to monitor the CID. Because of the geometry of the barrel, a horizontal non-interacting particle in the halo region traveling in the beam direction will traverse CID striking 11 crystals if it is displaced radially from the beam center line a distance between 11.0 cm and 18.5 cm. Shown in Fig. 12 is a typical pulse-height spectrum for one crystal for a halo data run. The minimum-ionizing-particle peak is used to calibrate the crystal. The energy deposit corresponding to this peak was determined from Monte Carlo data such as that shown in Fig. 13a which indicates that the expected energy deposit spectrum has a Landau distribution and peaks at about 31 MeV for the CIB crystals (shown) and 43 MeV for the longer CIR crystals.

In Fig. 13b is shown a crystal pulse-height spectrum where the pulse height was plotted only for those events for which 11 crystals in a row had energies above pedestal. The 11-collinear-crystal requirement ensured near axial trajectories. The fit shown is a Landau distribution broadened by a Gaussian resolution function. The fit is excellent, with a $\chi^2$/degree-of-freedom of 1.21. (Without the Gaussian resolution function the value for the $\chi^2$/degree-of-freedom was an unacceptable 4.5.) The resolution estimated from the fitted Gaussian width was 2.2 MeV. During each experimental

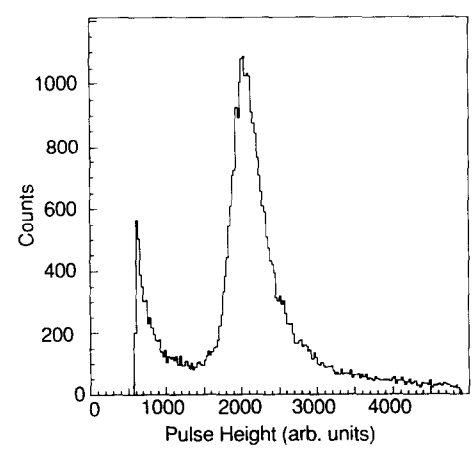


Fig. 12. Typical pulse height spectrum for a single CsI channel for a beam halo run.

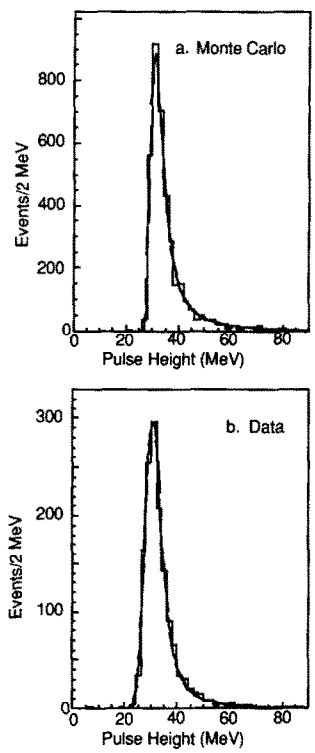


Fig. 13. Pulse height spectrum from a single minimum ionizing particle as (a) predicted by Monte Carlo and (b) observed in the data. The curves are Landau distributions broadened by a Gaussian resolution function.

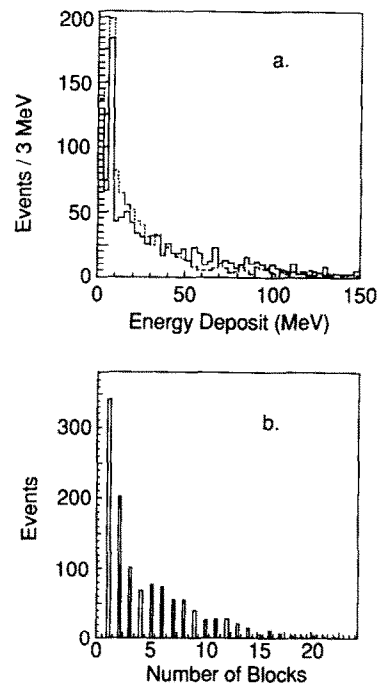


Fig. 14. (a) Distributions of energy deposited in the CsI detector by simulated recoil neutrons. The solid histogram is the total energy deposited and the dashed histogram is the maximum energy deposited in a single block. (b) The number of blocks with energy deposited for recoil neutrons.

running period the CsI array was calibrated twice with beam halo, once at the beginning of the run and once at the end. A comparison was made between the calibration constants obtained at the beginning and end of each run and it was observed that the gain for each channel typically varied by less than 5% over a six-month period.

### 4.2. Predicted neutron response

The primary motivation for the CID is its use as a detector in all-neutral final states. The intention is to veto events which have photons produced at large angles and thus miss the LGD. However, all-neutral events also have a recoil neutron which typically hits the CID. The expected sensitivity of the CID to neutrons has been determined by generating 5000 events of the type $\pi^- p \rightarrow n X^0$ with an exponential $t$-distribution for the neutrons of the form $d\sigma/dt = A e^{-3.0|t|}$. The neutrons were then processed through GEANT. A total of 1160 events deposited some energy in CID. The distribution of energy deposited is shown in Fig. 14a. In this figure, the solid line is the total energy deposited and the dashed histogram shows the distribution of the maximum energy deposited in a single block. Shown in Fig. 14b is the distribution for events with some deposited energy of the number of blocks with energy deposit. It is typical of these events that about half the time, one or two blocks "fire" with the remainder of the events having a rather high average multiplicity. The fact that the CID is sensitive to neutrons means that we will lose potential "good" events when we use the CID as an event veto to get rid of events with unwanted soft photons. With a threshold between 5 and 10 MeV which we expect to use for the CID, approximately 15% of the events with no photon striking the CID will be vetoed by the neutron response.

### 4.3. Isolation of neutron recoils

A sample of $\pi^- p \rightarrow \pi^- \pi^+ X^0$ events from the 1994 data run was studied to determine the effectiveness of CID in selecting a sample of events where the only recoiling particle was a neutron. A charged trigger was used to verify the effectiveness of CID because of its superior missing-mass resolution, allowing us to observe the effect of CID on the $\Delta^0(1232)$ shoulder in a missing-mass spectrum. In addition, this topology was studied extensively by Grayer et al. [12] using a veto similar in function to CID, providing a straightforward comparison with data taken by our experiment.

Each event in the sample met the following requirements. Two outgoing tracks of opposite charge were required. The cylindrical drift chamber, CDC, surrounding the hydrogen target contained no hits in its outermost cylinder. Any hits

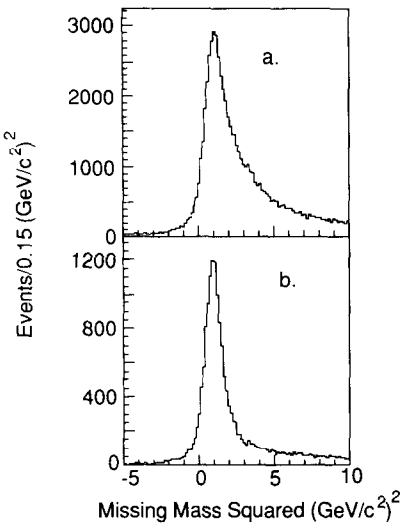


Fig. 15. (a) Missing-mass-squared distribution for events with two outgoing charged tracks. (b) Missing-mass-squared distribution for events included in (a) which have no energy deposit in the CsI detector.

in the LGD were required to be associated with one of the two charged tracks in the final state. Finally, the vertex of each event was required to be within the hydrogen target.

Shown in Fig. 15a is the two-pion missing-mass-squared distribution without the CsI veto requirement. Fig. 15b shows the two-pion missing-mass-squared distribution with a CsI veto cut requiring less than 20 MeV to be in the entire CsI array. With the CsI cut the missing-mass-squared distribution changes dramatically. When Fig. 15b is fit to a Gaussian plus a polynomial background, the peak of the Gaussian is centered at 0.88 GeV$^2$, consistent with a pure sample of recoil neutrons.

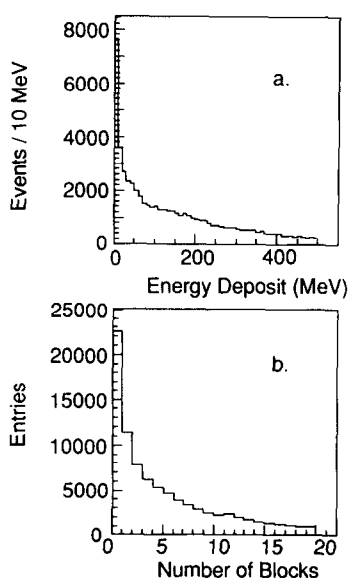


Fig. 16. (a) Distributions of total energy deposited in the CsI detector for all-neutral triggers. (b) The number of blocks per event with energy deposited for neutral events.

### 4.4. Response to all-neutral events

All-neutral triggers were taken in the 1994 run vetoing with scintillation counters downstream of the target region. Requiring in addition that no charged particles were present in the cylindrical drift chamber surrounding the target, an event sample was obtained which shows how the CID responds to all-neutral events. Shown in Fig. 16a is the total energy deposited in the CID. In Fig. 16b the distribution of the number of blocks which contain energy is plotted. These figures can be compared with those of Fig. 14 which is the Monte Carlo prediction for events with a neutron recoil which will be a subset of the all-neutral events used in the figure.

### 4.5. Response to low energy protons

To understand the effect of protons on CID a comparison was made between the tracks found in the cylindrical tracking chamber (CDC) surrounding the hydrogen target and the cluster location in CID. A large sample of events was examined in which each event was required to have a single track in CDC. In addition, three forward outgoing tracks were required, two of which had negative charge and one

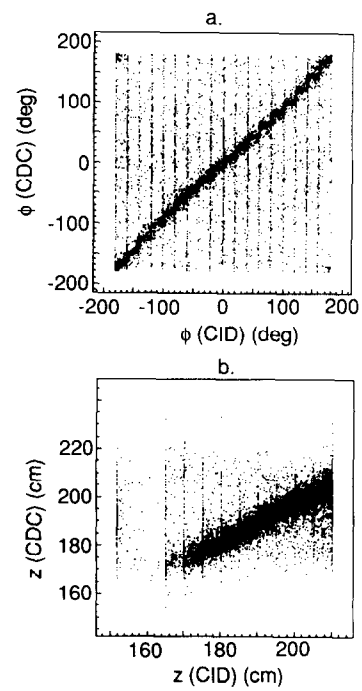


Fig. 17. Correlations of: (a) azimuth and (b) the $z$ coordinate for measurements made with the CsI detector (CID) and measurements made with the cylindrical drift chamber (CDC).

positive. The recoil track in CDC was then assumed to be (in most cases) a proton.

A simple cluster finder was used to find the azimuth ($\phi$) and the $z$-coordinate of the hit in CID. The cluster finder used a linear-weighted-mean technique. The cluster coordinates could then be compared with the ($\phi, z$) coordinates of the track detected in CDC. In Fig. 17 are shown the correlations between the $\phi$ and the z coordinates of the CDC track and the CID cluster location. Events were selected for which only a single cluster was present in CID with less than 6 blocks having energy deposit. The resolution of the CID in $\phi$ and z is on the order of the dimensions of a single block (5 cm in $z$, 20° in $\phi$) as expected. (The vertical line structure in Fig. 17 is caused by hits in a single block in CID in which case the hit is assumed to be in the center of the block, i.e. at a fixed $z$ and $\phi$.)

In those events in which the CDC $\phi$ and $z$ coordinates correlated well with the cluster in CID, the energy distribution was compared with Monte Carlo expectations for recoil protons. Data were examined for two different topologies: events with either one or three outgoing tracks plus a recoil. In Fig. 18 is shown the distribution of energy deposited in the CsI for the single-track data and for the three-track data. Protons were then generated using GEANT with $e^{-3|t|}$ and $e^{-7|t|}$ distributions. The distribution of energy deposited in CID for the Monte Carlo data is shown in Fig. 19. The Monte Carlo results show that the energy deposit distribution in the CID is a strong function of the momentum transfer distribution of the data. Those results show the structure of a straight-through peak superimposed on a broad structure caused by stopping protons (especially evident in Fig. 18a).

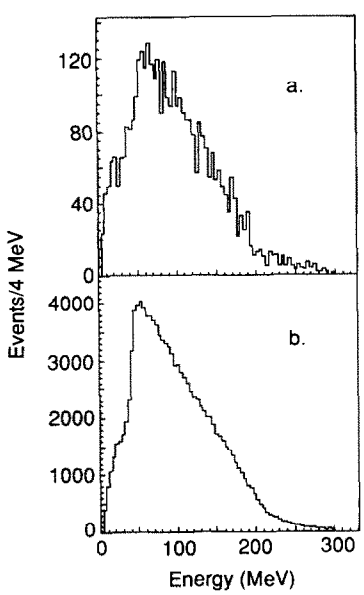


Fig. 18. Distributions of energy deposited in the CID for proton candidate tracks for (a) events with one fast forward outgoing track and for (b) events with three fast forward outgoing tracks.

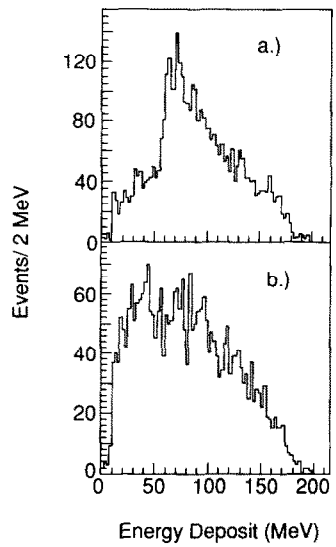


Fig. 19. Distributions of energy deposited in the CID for Monte Carlo recoil protons generated with $t$-distributions of (a) $e^{-3|t|}$ and (b) $e^{-7|t|}$

As can be seen in a comparison of Figs. 19 to Figs. 18, the data fall somewhere between the two extreme distributions exhibited in the Monte Carlo. A more detailed analysis is necessary to determine the exact t distribution needed to model the data correctly, but it is clear that the CID energy scale is approximately correct.

## 5. Results and conclusions

The mechanical and electrical design, construction, and performance of a 198-crystal CsI(Tl) detector designed to veto photons in an exotic-meson search at Brookhaven National Laboratory is described. Important design considerations for the array included operation in a 1 T magnetic field and good response to low-energy photons (down to energies of approximately 20 MeV). Data were taken over the course of two runs during the summers of 1993 and 1994. Using these data, it has been shown that the detector works well in isolating events with no missing photons and that the response of the detector to minimum ionizing particles as well as to slow protons is well described by Monte Carlo calculations. The energy resolution for minimum ionizing particles which deposit about 30 MeV in the crystals is 2.2 MeV and the threshold energy which was effective for the data was 10–20 MeV.

## Acknowledgements

We wish to acknowledge the assistance of the MPS staff and the AGS staff whose dedicated work made this project

successful. Design work by Jacques Negrin is gratefully acknowledged. Assistance in the electronic design was provided by Dr. Ernesto Gransch. This research was supported in part by the National Science Foundation, the U.S. Department of Energy and the University of Notre Dame.

## References

[1] B.B. Brabson et al., Nucl. Instr. and Meth. A 332 (1993) 419.
[2] E. Blucher et al., Nucl. Instr. and Meth. A 249 (1986) 201.
[3] E. Aker et al., Nucl. Instr. and Meth. A 321 (1992) 69.
[4] E. Blucher et al., IEEE Trans. Nucl. Sci. NS-32 (1985) 716.
[5] Z. Bar-Yam et al., Nucl. Instr. and Meth. A 357 (1995) 95.
[6] F. Binon, Hadron Spectroscopy Summer School (HSSC), (1990).
[7] I. Holl, E. Lorentz, G. Mageras (Munich, Max Planck Inst.), MPI-PAE/Exp-E1-185, Oct 1987.
[8] CsI(Tl) data calculated using semiempirical formulae derived by E. Massaro, G. Auriemma and E. Costa, Nucl. Instr. and Meth. 219 (1984) 134. The formula is accurate to better than 3% in the energy interval between 1.5 and 50 MeV.
[9] R. Burn et al., CERN DD/EE/84-1 (1986).
[10] The compound used was RTV 615 Silicone Rubber Compound supplied by GE Silicones, General Electric Co., Waterford, NY 12188.
[11] eV Products is a division of II-VI Incorporated, 375 Saxonburg Blvd. Saxonburg PA 16056.
[12] G. Grayer et al., Nucl. Phys. B 75 (1974) 189.